

Restricted dynamics in oriented semicrystalline polymers: Poly(vinylidene fluoride)Amelia Linares,^{1,*} Aurora Nogales,¹ Alejandro Sanz,¹ Tiberio A. Ezquerra,¹ and Marco Pieruccini²
¹*Instituto de Estructura de la Materia, CSIC, C/ Serrano, 121, 28006 Madrid, Spain*²*CNR, Istituto per i Processi Chimico-Fisici, Viale Ferdinando Stagno d'Alcontres 37, 98158 Messina, Italy*
(Received 12 February 2010; revised manuscript received 8 June 2010; published 2 September 2010)

The effect of confinement by crystals on the α relaxation, observed by dielectric broadband spectroscopy, in isotropic as well as in oriented semicrystalline poly(vinylidene fluoride), is analyzed on the basis of a new thermodynamic model. In both samples, it has been found that the average free-energy barrier, ΔF , for conformational rearrangements is of the same order of the dispersion barrier heights, $\delta(\Delta F)$, around ΔF , i.e., the increase in the barrier height in conformational rearrangement is accompanied by an increase in the heterogeneity of constraining conditions. At a given temperature T , the readjustment free energy is larger in the oriented sample. This fact might be ascribed to either an enhanced effectiveness of confinement in the amorphous region due to the decrease of the amorphous layer thickness in the stacks, or to a change of the mean chain orientation or both. In addition, it is worth noting that in oriented poly(vinylidene fluoride) the regions of cooperative rearrangement are significantly larger. Moreover, independent of orientation, the size of these readjusting regions increase upon decreasing T . This feature, which underlies the Adam-Gibbs approach for liquids, is pointed out for the first time from direct data analysis in the case of confinement enhanced cooperativity. In addition to the above analysis, the samples have been characterized by differential scanning calorimetry, wide angle x-ray scattering, and small angle x-ray scattering.

DOI: [10.1103/PhysRevE.82.031802](https://doi.org/10.1103/PhysRevE.82.031802)

PACS number(s): 82.35.-x, 77.84.Jd

I. INTRODUCTION

Miniaturization down to the nanoscale range of devices and physical systems in general, is almost always accompanied by the emergence of features which deviate significantly from the classical behavior characterizing large systems. Many of these features are still challenging the common sense, yet lacking a satisfactory settlement within well established theoretical frameworks.

Within the variety of materials where these anomalies may show up, polymers represent a very important class, due to their widespread application. Confinement effects, in particular, are rather commonly encountered as they can be observed to influence glass transition temperature [1–3], molecular mobility [4,5], phase behavior and morphology [6,7], molecular orientation [8], and crystallization behavior [9–11].

Confinement is usually classified as being of either physical or chemical nature. With regard to the effects on molecular motion, physical confinement is meant in general to originate from the volume restriction of the nanosystem, whereas chemical confinement refers to constraints due to chemical bonds [12]. In semicrystalline polymers, which are extensively exploited for commercial applications, physical and chemical restrictions are intrinsically connected. Indeed, the reduced segmental mobility characterizing the amorphous regions is not only due to their limited volume extension, imposed by the presence of the crystals at the borders, but also to both entanglements of the chains and the anchoring of the latter to the embedding crystal surfaces. The nature of these constraining mechanisms ultimately relates to chemical

bonds, that is, to chain connectivity. For this reason, it is expected that the manner in which confinement affects segmental motion depends on the existence of a mean chain orientation in the amorphous nanodomains. This aspect is in fact envisaged to be effective in the following analysis and will be discussed to some extent.

As a further basic aspect concerning confinement, there are two main features it shares with the glass transition process, namely, the existence of a long wavelength cutoff in the conformational fluctuation spectrum and the cooperative character of the molecular motion, the two being mutually connected [13].

In confined amorphous domains the origin of the wavelength cutoff is obviously related to the presence of crystalline domains at their borders; within the crystal indeed, the chain conformation is established by the crystal lattice. On approaching the glass transition from the liquid state, conformational fluctuations of large characteristic length scale become so slow to appear as frozen; in other words, the spectrum of the fluctuating modes reduces to the short wavelength region. The difference between the two cases is in that crystal confinement carries with it a spatial localization of the fluctuation modes, which is not present in a liquid approaching the glass transition on decreasing its temperature [13].

With regard to cooperativity in complex liquids, its character has been clearly formulated by Adam and Gibbs [14] through the concept of cooperatively rearranging region (CRR), defined as a subsystem which, upon a suitable thermodynamic fluctuation, is able to change its configuration into another independently of its environment. The CRR size increases as the temperature T decreases toward the glass transition value T_g . The presence of confining walls thus suggests that some influence on the glass transition process can be expected when the CRR size approaches the volume of the amorphous domain. It is indeed with this idea in mind

*alinares@iem.cfmac.csic.es

that several authors discussed the effect of confinement on the glass transition process (see e.g., Refs. [15–18]).

Also when cooperativity is enhanced by confinement, there are regions where rearrangements occur without changes at their borders. In this case, the set of monomers participating to a local chain conformational readjustment will be said to form a “static cooperatively rearranging region” (SCR). There is *a priori* no relation linking their shape and extension to characteristic lengths of the amorphous nanodomains, except that they cannot occupy a volume larger than the minimum available. Within a semicrystalline stack, for example, the amorphous layer thickness is an upper limit to the SCR size in the perpendicular direction to the basal planes. The following analysis shows that the size of the SCR increases with decreasing the temperature; that is, the SCR size does not in general coincide with whole (amorphous) host domain.

The present work is thus aimed at investigating some features of conformational dynamics under confinement, which are also found in glass formation processes. This is done by analyzing dielectric relaxation data by means of a statistical mechanical model developed recently [13].

Broadband dielectric spectroscopy (BDS) has been chosen in order to study the dynamic features of segmental motion and the effects of confinement on the dielectric function [19,20], because it is a comparatively simple technique for the analysis of the relaxation behavior over a suitable frequency interval. In the present study, we will concentrate on poly(vinylidene fluoride) (PVDF), which has shown to be a promising polymer to be processed at the nanometer scale [21,22]. The advantage of studying basic physical mechanisms on a well known system is evident. Besides, one of the appealing features of PVDF is that the central frequency of the segmental relaxation process (α process) does not change much upon drawing, thus allowing to investigate the combined effects of chain orientation and the associated morphological changes, without the need to vary the temperature in order to maintain the response profiles in the same frequency window {as an example, this is not the case of poly(ethylene terephthalate) [13,23]}.

II. EXPERIMENTAL

A. Materials

The polymer investigated was commercial PVDF (Solef 6010), delivered by Solvay (Germany) with $M_n=64\,000$ and $\rho=1.78\text{ g/cm}^3$. Films of thickness about $200\ \mu\text{m}$ were manufactured by compression molding in a Collins hydraulic press at 200 bar pressure for 5 min at $180\text{ }^\circ\text{C}$. Before any measurement, all samples were carefully vacuum dried at $80\text{ }^\circ\text{C}$ for 24 h. A home-made device, which was put into a Glass oven B-585 Drying (Büchi), was used to stretch PVDF, at $100\text{ }^\circ\text{C}$; a natural drawing ratio of $\kappa=4$ was obtained.

B. Techniques

1. Differential scanning calorimetry

Differential scanning calorimetry (DSC) experiments were carried out using a Perkin-Elmer DSC7 equipped with a

nitrogen cooling system. DSC measurements were performed under nitrogen environment and temperature and heat capacity were calibrated using indium. The samples were encapsulated in aluminum pans and the typical sample weights used in these experiments were between 5 and 10 mg. The thermal characterization of the PVDF samples was carried out in two different steps depending on the temperature range of interest. Low temperature scans from -100 to $5\text{ }^\circ\text{C}$ at $10^\circ/\text{min}$ were performed to estimate the glass to liquid transition temperature T_g . Moreover, in order to explore the melting behavior, heating cycles from 40 to $195\text{ }^\circ\text{C}$ at $10^\circ/\text{min}$ were monitored.

The values of T_g were estimated during the first heating run in order to maintain the thermal and structural history of the materials. The T_g 's were computed following the midpoint criterion (middle point of the temperature interval defined by the intersection between the glass with midpoint tangent and liquid with midpoint tangent, respectively). In addition to that, the melting enthalpies ΔH of the PVDF samples were calculated from the area underneath the endothermic peak observed during the heating scans between 40 and $195\text{ }^\circ\text{C}$. The values of ΔH associated to the melting process were also estimated during the first heating scan of the materials.

2. X-ray scattering experiments

Wide angle x-ray scattering (WAXS) measurements were performed by means of a Seifert XRD 3000 θ/θ diffractometer using Ni-filtered Cu $K\alpha$ radiation ($\lambda=0.154\text{ nm}$) at a scanning speed of $0.02^\circ/\text{s}$. The fraction of the crystalline phase (X_c^{WAXS}) can be estimated, by using a curve-fitting program, from the ratio of the area below the crystalline peaks to the total area of the diffractogram [24].

Small angle x-ray scattering (SAXS) experiments have been accomplished by a NanoSTAR-U system by Bruker using Cu $K\alpha$ radiation ($\lambda=0.154\text{ nm}$) equipped with a three pin-hole collimation system, cross-couple Göbel mirrors and a Hi-Star multiwire area detector. The SAXS data have been corrected for background scattering by considering the absorption coefficient. Reciprocal space calibration has been done using collagen as standard.

3. Dielectric spectroscopy

For the dielectric experiments sandwich geometry was used. Circular gold electrodes, 2 cm in diameter, were deposited onto the film surfaces by sputtering. Measurements of the complex dielectric permittivity, $\epsilon^*=\epsilon'-i\epsilon''$, were performed over a frequency window of 10^{-1} – 10^7 Hz and in a temperature range of $-150\text{ }^\circ\text{C}$ to $+150\text{ }^\circ\text{C}$. To cover the above frequency range, a Novocontrol spectrometer integrating an ALPHA dielectric interface was employed with a precision in $\tan\delta=\epsilon''/\epsilon'=10^{-5}$. In these experiments, the temperature was controlled by a nitrogen jet (QUATRO from Novocontrol) with a temperature error, during every single sweep in frequency, of $\pm 0.1\text{ }^\circ\text{C}$.

The dielectric relaxations were empirically described in terms of the Havriliak-Negami (HN) equation [25],

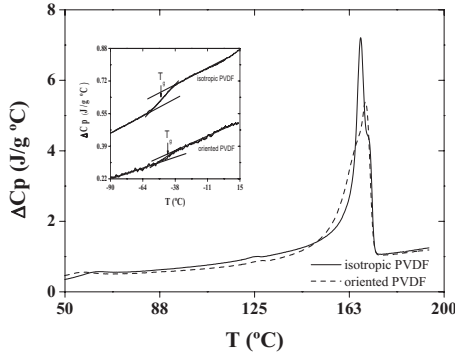


FIG. 1. Variation of heat capacity with temperature for isotropic and oriented PVDF. Inset displays the region of the glass transition temperature.

$$\varepsilon^* = \varepsilon'(\omega) - i\varepsilon''(\omega) = -i \frac{\sigma_0}{(\varepsilon_0\omega)^s} + \varepsilon_\infty + \sum \frac{\Delta\varepsilon}{[1 + (i\tau_{HN}\omega)^b]^c}, \quad (1)$$

where ε^* , ε' , and ε'' are the complex, real and imaginary components of the dielectric permittivity, respectively; $\Delta\varepsilon = \varepsilon_s - \varepsilon_\infty$ (where ε_s and ε_∞ are the dielectric constants at limiting low and high frequencies, respectively) is the relaxation strength; σ_0 is the dc conductivity; ε_0 is the dielectric constant of vacuum; ω is the angular frequency; τ_{HN} is the central value of the relaxation time distribution function, and b and c ($0 < b, c < 1$) are shape parameters which describe the broadening and the symmetry of the relaxation time distribution function, respectively. Conductivity is usually associated with generation and transport of polarization-induced charges through the polymer under the action of an electric field; the exponent s in the dc contribution characterizes the nature of the conduction process [26].

III. RESULTS

A. Thermal characterization of oriented and isotropic PVDF

Figure 1 represents heating thermograms of isotropic and oriented PVDF between 50 and 195 °C. Both materials show a small endothermic transition around 125 °C, which has been previously associated to translational and rotational motions of the chains in the crystalline regions and considered by some authors as a premelting peak [27,28]. At higher temperatures, the main melting peak can be observed in both cases, being the maximum located at 167 and 169 °C for isotropic and oriented PVDF respectively. To calculate the degree of crystallinity we used Eq. (2) which implies integration of the calorimetric curve,

$$x_c = \frac{\int_{T_i}^{T_f} (dH/dT)dT}{\Delta H_0} \times 100, \quad (2)$$

where ΔH_0 is the ideal melting enthalpy of 100% crystalline PVDF (104.5 J/g), while T_i and T_f define the temperature interval associated to the main melting peak [29]. The degrees of crystallinity obtained in this way are 41 and 46% for

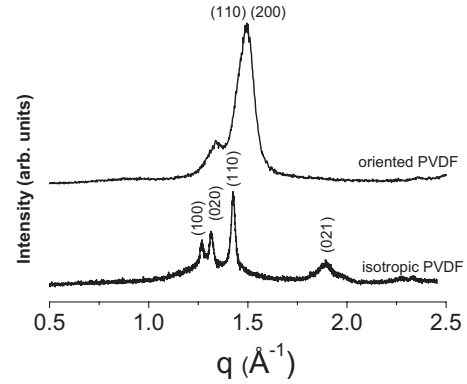


FIG. 2. Wide-angle x-ray diffractograms for isotropic and oriented PVDF.

isotropic and oriented PVDF respectively. The inset in Fig. 1, shows the evolution of the relative C_p of PVDF samples as a function of temperature at a heating rate of 10 °C/min. The midpoint of the T_g was taken as criterion to estimate the glass transition temperature. Reliable T_g values were obtained, despite the weak step of the C_p associated to the glass transition. The midpoint T_g for isotropic and oriented PVDF is -47 and -36 °C, respectively. This indicates that the dynamics of the amorphous fraction in the oriented PVDF is more restricted than that in the isotropic sample.

B. Structural characterization

Figure 2 shows the WAXS patterns obtained at room temperature, as a function of the scattering vector q [$q = 4\pi/\lambda(\sin \theta)$, λ being the wavelength and 2θ the scattering angle], for original PVDF (isotropic sample) and stretched PVDF (oriented sample). The diffraction patterns of isotropic and oriented PVDF exhibit the characteristic Bragg peaks corresponding to the α and β crystalline phases [30], respectively. The indexes of the main reflections are indicated in the figure.

As illustrated in Fig. 3, the two-dimensional (2D) scattering patterns obtained from SAXS experiments can be azimuthally integrated in order to obtain the one-dimensional (1D) scattering intensity as a function of the scattering vector

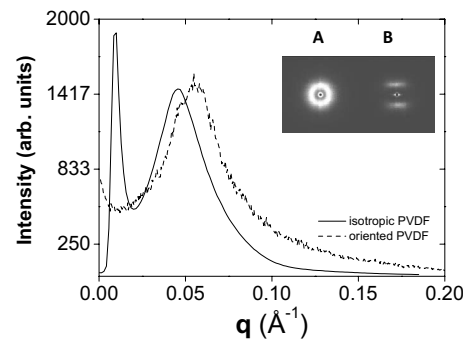


FIG. 3. Sliced meridional linear intensity profiles from the SAXS patterns for isotropic and oriented PVDF samples. The insets A and B are the 2D patterns corresponding to isotropic and oriented PVDF, respectively.

TABLE I. Fraction of crystalline phase and structural parameters for the investigated samples. X_C^{DSC} and X_C^{WAXS} fraction of crystalline phase obtained from DSC and WAXS, respectively. L : long spacing derived by different methods; l_c and l_a : thickness of the crystalline and amorphous layers, respectively, and X_L : linear crystallinity ($X_L = l_c / (l_c + l_a)$), determined from SAXS experiments.

SAMPLE	X_C^{DSC}	X_C^{WAXS}	L_b (Å)	L_c^M (Å)	L_c^m (Å)	l_c (Å)	l_a (Å)	X_L
Isotropic PVDF	41	33	113.25	101	84	68.62	32.38	68
Oriented PVDF	46	41	93.80	92	66	69.49	22.51	76

q [31]. In the case of the isotropic PVDF the SAXS pattern (A-photograph in the inset of Fig. 3) consists of an isotropic ring with single scattering maximum, indicating random orientation of the crystalline domains in the sample. The linear 1D slices were extracted along the meridional direction of the 2D SAXS patterns. When PVDF is stretched (B-photograph in the inset of Fig. 3), the SAXS pattern becomes anisotropic, and two elongated scattering lobules appear along the meridian, together with a sharp scattering streak along the equator. The meridional SAXS maxima indicate that the crystalline domains underwent reorientation forming layered lamellae aligned, on average, perpendicular to the stretching direction. The equatorial SAXS streak reveals that the lamellae assemble themselves into an incipient microfibrillar structure [32]. Since the SAXS pattern of oriented PVDF exhibits cylindrical symmetry, a projection operation was applied to obtain the integrated intensity on the meridian [$I_1(q_3)$] using the expression,

$$I_1(q_3) = \int_0^\infty I(q_{12}, q_3) q_{12} dq_{12}, \quad (3)$$

here, the subscript 12 and 3 represents the equatorial and meridional direction respectively (see B pattern in the inset of Fig. 3). From Fig. 3, the position of the meridional maximum, q_m , can be located at $q \approx 0.046 \text{ \AA}^{-1}$ and $q \approx 0.056 \text{ \AA}^{-1}$, for isotropic and oriented PVDF, respectively. The values corresponding to the long period, L_b , are related to the meridional maximum by,

$$q_m = 2\pi/L_b \quad (4)$$

The L_b values, which characterize the average distance between the gravity center of consecutive crystalline lamellae, are compiled in Table I.

In order to get more complete information on the lamellar structure of the system, the correlation function formalism was applied to the integrated intensity. To obtain the correlation function, a 1D Fourier transformation was applied to $I_1(q_3)$ according to,

$$\gamma(X) = \frac{\int_0^\infty I_1(q_3) \cos(q_3 X) dq_3}{\int_0^\infty I_1(q_3) dq_3} \quad (5)$$

The results of this formalism are displayed in Fig. 4. In addition to the long spacing calculated by application of Bragg's law [Eq. (4)], the correlation function formalism gives additional information of the long spacing: a) from the position of the first maximum (L_c^M) and b) from twice the position of the first minimum (L_c^m). From all these parameters, it is possible to draw some conclusions on the width of the thickness distribution of the two phases present in the system. As pointed out by Strobl *et al.* [33] for an ideal 1D two-phase model system, $L_c^M = L_c^m$. The average linear degree of crystallinity in the lamellar stacks can be determined from the following equation,

$$\frac{B}{L_c^M} = x_1 x_2, \quad (6)$$

where B is the first intercept of $\gamma(r)$ with the abscissa, and x_1 and x_2 are the volume fractions of the two phases, within the lamellar stacks, respectively, ($x_1 + x_2 = 1$). The thickness of the two phases can be calculated as $l_1 = x_1 L_c^M$ and $l_2 = x_2 L_c^M$. There has been some controversy in the literature with regard to the assignment of l_1 and l_2 to the crystalline and amorphous phases.

Table I shows the values for the long spacing obtained by application of Bragg's law and the correlation function formalism. The assignment of the thicknesses for amorphous and crystalline thicknesses has been made on de basis of the linear crystallinity within the stacks which can take either the value of $X_L = l_1 / (l_1 + l_2)$ or $X_L = l_2 / (l_1 + l_2)$. The values reported in Table I make the derived values for X_L to be higher than the experimental ones estimated by DSC measurements.

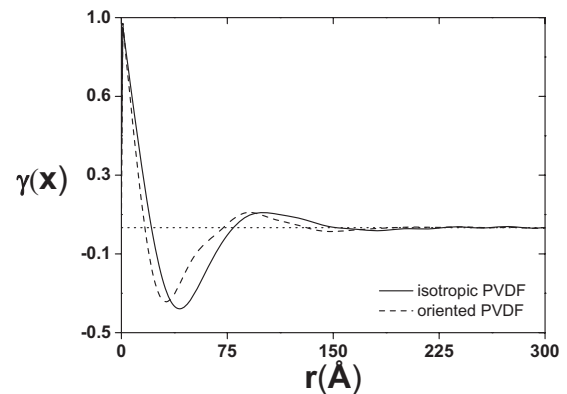


FIG. 4. Correlation function obtained from the meridional SAXS projected intensity for isotropic and oriented PVDF:

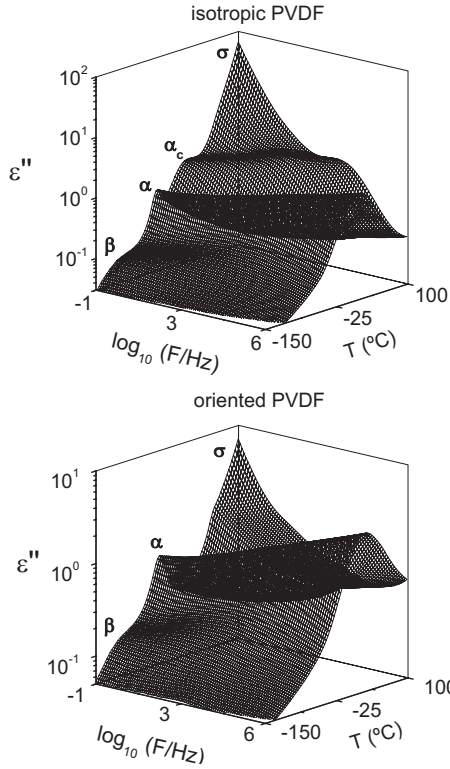


FIG. 5. ϵ'' values for isotropic and oriented PVDF as a function of frequency and temperature.

This is consistent with the fact that in the case of the oriented sample the molecular chains become aligned, more densely packed, and the crystallinity increases. It is worth to point out that the thickness of the amorphous lamina regions is lower than that of isotropic PVDF.

C. Broadband dielectric spectroscopy

Dielectric loss values, ϵ'' , measured as a function of temperature and frequency, for isotropic and oriented PVDF, are presented in Fig. 5. According to previous literature [34,35], the crystalline α phase of PVDF, which corresponds to isotropic PVDF, presents three main dielectric relaxations labeled as β , α , and α_c in the order of increasing temperature. The relaxation processes appear as maxima in ϵ'' vs log frequency, drifting toward higher frequencies as temperature increases. Additionally a conductivity contribution is also detectable at low frequencies for the higher temperature data. The α_c process has been attributed to a relaxation in the crystalline region of the α crystalline phase of PVDF. The intense α process has been associated to the segmental dynamics of the amorphous phase. The lower temperature β process has been associated to local dynamics related to polar groups in the amorphous phase [34,35]. The α_c process in oriented PVDF, whose crystalline fraction mainly consists of the crystalline β phase, is not observed.

Figure 6 and 7 show the dielectric loss values for the α and β relaxations, respectively, as a function of frequency at different temperatures. The solid lines represent the best fits calculated by applying Eq. (1). The fitting procedure in-

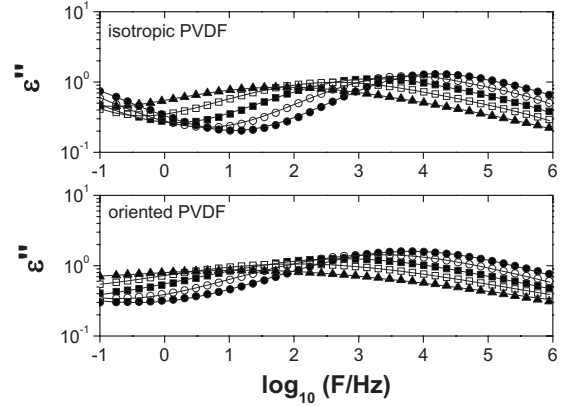


FIG. 6. Dielectric loss evolution of α relaxations for isotropic and oriented PVDF, with frequency at: ● -15 °C; ○ -20 °C; ■ -25 °C; □ -30 °C; and ▲ -35 °C. Solid lines correspond to the best fitting to Eq. (1).

involved fitting the β relaxation at low temperatures to a single Havriliak-Negami process. At higher temperatures, the α relaxation was fitted using a fixed shape parameter c ($c=1$). The contribution of the β relaxation at high frequencies was taken into account by extrapolating the low temperatures shape parameters and relaxation time [36,37]. Figure 8 illustrates the relaxation time for the α and β relaxations, τ_{max} , as a function of the reciprocal temperature. As shown, in both cases the β relaxation exhibits Arrhenius behavior, as expected for a subglass relaxation process [38]. The α process displays a curvature characteristic of a Vogel-Fulcher-Tamman (VTF) dependence of the type,

$$\tau_{max} = \tau_0 \exp \left[\frac{DT_0}{(T - T_0)} \right], \quad (7)$$

where τ_0 is a characteristic time (experimental data indicate that for many systems $\tau_0 \approx 10^{-14}$ s [39-42]), T_0 is the Vogel temperature and D is the fragility strength parameter [43]. This behavior is characteristic of cooperative segmental motions appearing above the glass transition temperature. The

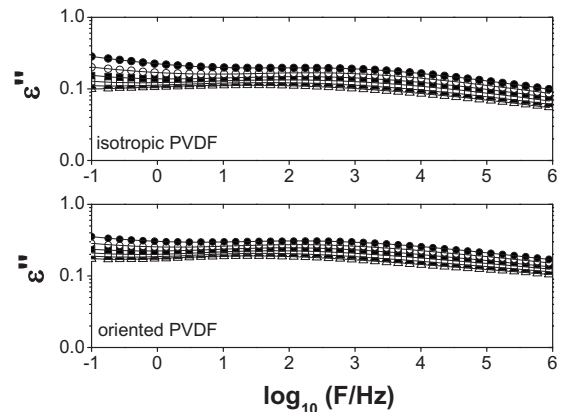


FIG. 7. Dielectric loss evolution of β relaxations for isotropic and oriented PVDF, with frequency at: ● -55 °C; ○ -60 °C; ■ -65 °C; □ -70 °C; ▲ -75 °C; and △ -80 °C. Solid lines correspond to the best fitting to Eq. (1).

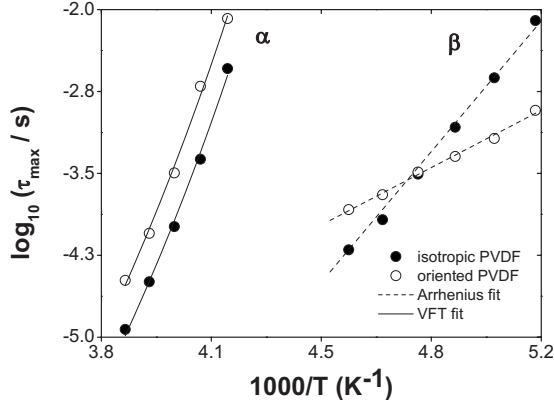


FIG. 8. Dependence of the relaxation time of the α and β relaxations as a function of the reciprocal temperature for isotropic and oriented PVDF.

parameters obtained for isotropic and oriented PVDF are compiled in Table II and the solid lines in Fig. 8 represent the best fits of α process according to Eq. (7).

A convenient method to estimate the fragility of glass forming liquids [39–41] consists of calculating the fragility index,

$$m = \frac{d \log_{10} \tau}{d(T^*/T)_{T=T^*}} \ln 10, \quad (8)$$

where, by definition, the reference dielectric glass transition temperature, T^* , is the temperature at a relaxation time (τ^*) equal to 100 s [44,45].

From Eqs. (7) and (8), a relation between m and D can be obtained [46]:

$$D = \frac{m_{\min}^2}{m - m_{\min}} \ln 10 \quad (9)$$

with $m_{\min} \equiv \log_{10}(\tau^*/\tau_0) \approx 16$. The parameters obtained are compiled in Table II. As shown, although both samples present very similar values, the fragility index, m , is slightly larger for the isotropic PVDF. Recent theoretical studies based on a generalized entropy theory [47,48] have linked the fragility to the packing efficiency of polymers with various complex structures in the glassy state. Under this framework, an enhanced molecular packing and a corresponding decrease of the relative length scale of cooperative segmental motions, would lead to reduced fragility of the glass formation. Therefore, the changes of the molecular packing induced by the drawing of the disordered chains in the oriented

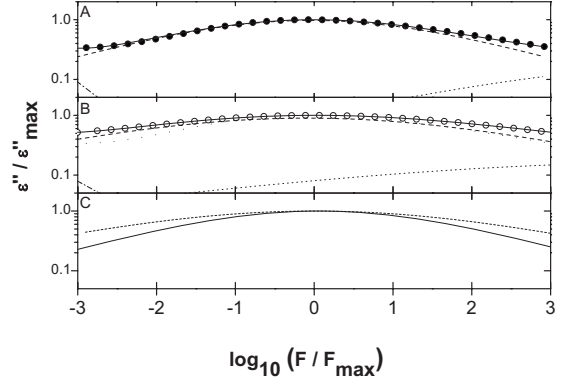


FIG. 9. Normalized $\epsilon''/\epsilon''_{\max}$ ratio vs $\log(F/F_{\max})$ for isotropic (a) and oriented (b) PVDF at $T=-30^\circ\text{C}$. The continuous lines are HN fits according to Eq. (1) and dashed, dotted, dash-dotted lines correspond to α , β and conductivity contributions, respectively. Plot C shows the Havriliak-Negami fit corresponding to the α contribution, for isotropic (solid line), and oriented (dash line) PVDF.

PVDF should decrease the fragility of the glass formation as observed here experimentally by dielectric relaxation measurements. In any case, both systems can be considered physically similar from the point of view of fragility. The differences between dielectric and calorimetric glass transition temperature can be ascribed to the fact that the T^* is obtained by extrapolation of dielectric relaxation times to $\tau=100$ s, over more than 4 orders of magnitude.

In order to compare the α relaxation for isotropic and oriented PVDF, normalized dielectric loss data $\epsilon''/\epsilon''_{\max}$ have been plotted in Fig. 9 as a function of a normalized frequency F/F_{\max} . Here, ϵ''_{\max} is the maximum value of ϵ'' and F_{\max} is the corresponding frequency. In Fig. 9, the different contributions of the β relaxation, at higher frequencies, and of the conductivity, at lower frequencies, have been included. The lower panel of Fig. 9 shows the α relaxation contribution of both isotropic and oriented PVDF for the sake of comparison. A significant broadening of the α relaxation is observed for oriented PVDF.

In principle, it is possible to discuss the observations related to the α processes by resorting to the concept of CRR, initially introduced by Adam and Gibbs [14]. This point is considered in the following section.

IV. APPROACH TO THE SEGMENTAL RELAXATION ANALYSIS: THEORETICAL BACKGROUND

In the present section, the basic aspects of a mean-field statistical mechanical model describing segmental relaxation

TABLE II. Calorimetric glass transition temperature and Vogel-Fulcher-Tamman parameters for the investigated samples.

SAMPLE	T_g^{DSC} (K)	τ_0 (s)	T_0 (K)	D	m	T^* (K) ^a
Isotropic PVDF	226	10^{-14}	162.4	12.2	64	216.3
Oriented PVDF	237	10^{-14}	161.1	13.1	60	218.5

^a T^* (K) is defined at $\tau=100$ s.

in confined regimes are outlined; details can be found in Ref. [13].

A. Segmental relaxation in confined regimes

Consider a small amorphous region embedded by crystals; from the statistical thermodynamic point of view, the degrees of freedom associated to this limited domain can be divided into two main classes. The first one (class C) collects all those conformational modes which are affected by the finiteness of the volume available for conformational fluctuations and/or by entanglement and pinning to the crystals via chain connectivity. The other (class V) consists of all the modes (e.g., vibrations, β relaxations, short length modes) which are not significantly influenced by confinement. These two classes indeed represent two different, mutually interacting subsystems.

When confinement by crystals dominates, the thermodynamic fluctuations among the degrees of freedom pertaining to class C, can only be induced by the (weak) interaction with the comparatively faster modes of class V. The reason is that the long-range conformational motions cannot propagate outside the confined region (since for example the density within the crystals is a constant), so that the direct interaction of these modes with the heat bath is hindered.

Confinement enhances the character of cooperativity of the segmental motion; the set of monomers participating to a local chain conformational readjustment will be said to form a SCRR to make a distinction from the CRRs introduced by Adam and Gibbs [14]. These authors, indeed, consider only the cooperativity associated to the freezing of long range modes in a liquid approaching the glass transition [13]. In the present context, the shape, size and relaxation features of the cooperatively rearranging regions arise from both chain dynamics, such as in the Adam-Gibbs scheme, and crystal confinement (supposedly dominant). As a mean-field-like approximation, we shall consider all SCRRs in the system as consisting of the same number z of monomers.

In a small amorphous region of volume V , the constraints rule out some conformational states; the actual partition function Z'_u is then smaller than in the absence of restrictions; as a further effect of confinement, not all fluctuations are able to cause conformational rearrangements. Let Z_c be the reduced partition function collecting only the states of Z'_u which allow a conformational change (i.e. $Z_c < Z'_u$); then, a free-energy threshold ΔF has to be overcome in order that a conformational readjustment can be reached, in a constrained system described by Z'_u [13,14],

$$\Delta F = -k_B T \ln \left(\frac{Z_c}{Z'_u} \right), \quad (10)$$

where k_B is the Boltzmann constant and T is the absolute temperature. The free-energy barrier ΔF refers to the whole SCRR; the character of cooperativity in this rearranging domain will be accounted for by associating to each monomer of the SCRR the same (specific) partition function $[Z'_u]^{1/z}$ and, for the reduced partition function,

$$Z \equiv Z_c^{1/z}. \quad (11)$$

The volume of the whole amorphous component of the semicrystalline system does not fluctuate and is thought to be composed of a (huge) number of SCRRs, whose partition function we take in the canonical form. Hence, following Ref. [14] as a guideline, the presence of the constraints will be accounted for by the existence of a minimum energy threshold per monomer, ζ , below which a thermodynamic fluctuation cannot produce a conformational readjustment. On the other hand, in principle, states with arbitrarily large energy values are still available for the SCRR, like for a nonconstrained canonical subsystem.

The calculation of Z is a rather complex task; for our purposes, however, it is taken in the following phenomenological form,

$$Z \equiv Z_{\zeta,n} \equiv \int_{\zeta}^{+\infty} dE \rho_E E^n e^{-E/k_B T}, \quad (12)$$

where n is an integer to be adjusted afterwards during data fitting and ρ_E is a constant (with the dimensions of an energy to the power of $n+1$) which will eventually turn out to be irrelevant [13].

Upon increasing n , the partition function $Z'_u = [Z_{\zeta,n} |_{\zeta=0}]^z$ describes an ever more constrained SCRR, consistently with the Adam and Gibbs scheme adopted here [14]. Indeed, the latter is based on the idea that the constraints quench the low energy, long-range modes. This is to say that the states accessible to a SCRR must correspond on average to energies of ever increasing value, as the restrictions become more effective. In this respect, the probability distribution $\rho_E E^n e^{-E/k_B T} / [Z'_u]^{1/z}$ describes this feature. The enhancement of crystal confinement (e.g., the isotropic vs oriented condition) and/or the long-range mode quenching (e.g., by a decrease in T) then cause an increase of n .

Of course Eq. (12), although reasonable, remains an assumption, and further improvements or insights concerning $Z_{\zeta,n}$ will be the subject of future work. By now, since the paper is focused on the SCRR transitions among the states forming Z'_u , with given average constraints (i.e., a given n arising from the actual measurement temperature and sample elongation), a $Z_{\zeta,n}$ form as given by Eq. (12) will be considered sufficient.

Taking a SCRR as a whole, it is important to point out that $\Delta F(\zeta)$ is a function of its actual chain conformation. On the other hand, once a readjusting fluctuation has occurred, the final conformational state of the SCRR is not unique in general and further readjustments will be characterized by different $\Delta F(\zeta)$ values. This means that in a stationary state, the whole amorphous component of a semicrystalline polymer is characterized by a distribution of monomers belonging to SCRR's with different levels of restriction. This distribution has been derived in Ref. [13] on the basis of general thermodynamic arguments and is given by,

$$P(\zeta, \lambda, n) = N(\lambda, n) \left(\frac{Z_{\zeta,n}}{Z_{0,n}} \right)^{\lambda k_B T} \exp \left\{ - \frac{1}{k_B T} \frac{Z_{\zeta,n+1}}{Z_{\zeta,n}} \right\}, \quad (13)$$

where $N(\lambda, n)$ is the normalization factor and λ is the Lagrange multiplier associated to the stationarity of the average rearrangement chemical potential barrier,

$$\begin{aligned}\overline{\Delta\mu} &\equiv \int_0^{+\infty} d\zeta \left[-k_B T \ln \left(\frac{Z_{\zeta,n}}{Z_{0,n}} \right) \right] P(\zeta, \lambda, n) \\ &= - \frac{\partial}{\partial \lambda} \int_0^{+\infty} d\zeta P(\zeta, \lambda, n).\end{aligned}\quad (14)$$

Equation (14) expresses implicitly the relationship between λ and $\overline{\Delta\mu}$.

An important result connected with the existence of the constraints distribution P , Eq. (13), is that the mean readjustment free energy $\Delta F \equiv z \overline{\Delta\mu}$ and its dispersion around the mean [13],

$$\delta(\Delta F) \equiv z \delta(\overline{\Delta\mu}) = z \left(- \frac{\partial \overline{\Delta\mu}}{\partial \lambda} \right) \quad (15)$$

(i.e., the heterogeneity of constraints) are inter-related: there is no finite ΔF without an heterogeneity. In fact it is always found by data analysis that [13,23],

$$\Delta F \approx \delta(\Delta F) \quad (16)$$

(see the analysis below). This is indeed an important relation, because it makes possible to derive the mean chemical potential increase of the amorphous regions, due to the rearrangement barrier, from the knowledge of both the central relaxation time τ_{HN} and the heterogeneity of the process, i.e., the width b of the corresponding Havriliak-Negami term.

From the knowledge of the distribution P it is possible to write the conformational relaxation function ϕ of the constrained amorphous regions. To this aim, we associate to each SCRR, that is, to each of its monomers characterized by the same ζ , the relaxation time,

$$\tau(\zeta) \equiv \tau^* e^{\Delta F(\zeta)/k_B T} = \tau^* \left(\frac{Z_{0,n}}{Z_{\zeta,n}} \right)^z, \quad (17)$$

where τ^* is an average (fast) characteristic time associated to the fluctuations within the class V subsystem which, as illustrated at the beginning of this subsection, are eventually responsible of the conformational fluctuations. Then, from Eqs. (13) and (17), we may describe the relaxation dynamics among the conformational states by means of the following form of the relaxation function:

$$\phi(\lambda, \tau^*, z, n; t) \equiv \int_0^{+\infty} d\zeta P(\zeta, \lambda, n) e^{-t/\tau(\zeta)} \quad (18)$$

where t is the time.

B. Analysis of the Havriliak-Negami representation of the α processes

All parameters in last equation (i.e., λ , τ^* , z , and n) have a well defined physical meaning. Upon adjusting them in order to reproduce the relaxation dynamics described empirically by the Havriliak-Negami function, we obtain a physical picture of the α process.

As a first step, we derive the relaxation function associated to a Havriliak-Negami term $\varepsilon_\alpha(\omega)$ by means of a Fourier cosine transform [49],

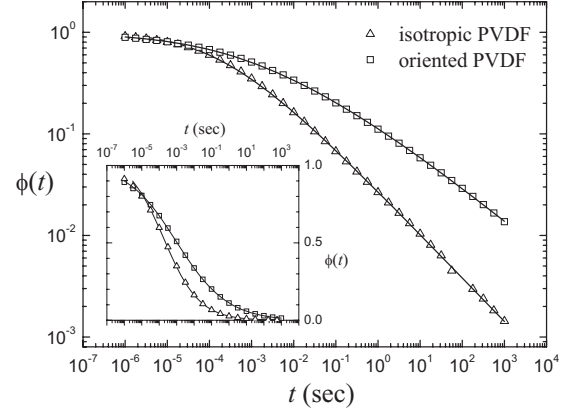


FIG. 10. Decay function associated to the α processes as obtained by Eq. (10) with the Havriliak-Negami parameters listed in Tables III and IV for $T = -30^\circ \text{C}$. The associated best fitting curves, solid lines represent $\Phi(t)$ as expressed by Eq. (20). The inset reports the same in linear ordinates (part of the symbols have been dropped for a better clarity of the figure).

$$\phi_\alpha(t) = \frac{2}{\pi} \int_0^{+\infty} \frac{\varepsilon_\alpha''(\omega)}{\Delta\varepsilon_\alpha} \cos(\omega t) \frac{d\omega}{\omega} \quad (19)$$

then, Eq. (18) is fitted to Eq. (19). The procedure is reported in detail in Ref. [13].

Once the fitting parameters are found, the distribution of Eq. (13) can be used to calculate $\Delta F = z \overline{\Delta\mu}$ [cf. Eq. (16)], the energy threshold $\bar{\zeta}$ and the corresponding deviations around the mean, $\delta(\Delta F)$ and $\delta\zeta$, respectively, by simple integration.

Figure 10 shows the relaxation functions derived at $T = -30^\circ \text{C}$ from the PVDF samples, together with the best fitting curves obtained from Eq. (18).

Before closing this section, a brief comment on error propagation may be of interest. The relationship between the Havriliak-Negami and the fitting parameters of the model is highly non-linear; thus, a selected case will be considered to show how the latter are sensitive to small changes of the former. Considering the case of isotropic PVDF at $T = -25^\circ \text{C}$, relative deviations of 5% to either b or τ_{HN} (but not to both at the same time) are imposed; then, the relative changes in z and τ^* are found to be around 10%, while for ΔF a relative variation of less than 5% is observed. The case of oriented PVDF at the same temperature is quite similar.

V. DISCUSSION

Table III reports the fitting results for the relaxation functions characterizing the isotropic PVDF sample at different temperatures. We first note the significant progressive increase of z as the temperature decreases. This, together with the systematic changes of the worked out n values [see the paragraph following Eq. (12)], suggests that the SCRR's size extracted from the analysis is not determined only by the volume rendered available by the crystals for conformational fluctuations, but also that some long-range modes progressively freeze on decreasing the temperature.

As T decreases we observe a steady increase of ΔF . This is directly connected with the decrease of the probability that

TABLE III. Measurement temperature T , width parameter b_α , central relaxation time τ_α , relaxation function parameters (λ , τ^* , z , and n) and free energy ΔF for an SCRR rearrangement, associated to the α processes in isotropic semicrystalline PVDF; the dispersion $\delta(\Delta F)$, the average minimum energy threshold $\bar{\zeta}$ and its dispersion around the mean $\delta\zeta$, as calculated from the fitting parameters using the distribution Eq. (14) are also reported.

T (°C)	b	τ_{HN} (sec)	τ^* (sec)	λ (kcal/mol) ⁻¹	z	n	ΔF (kcal/mol)	$\delta(\Delta F)$ (kcal/mol)	$\bar{\zeta}$ (kcal/mol)	$\delta\zeta$ (kcal/mol)
-15	0.55	1.2×10^{-5}	3.5×10^{-7}	1.47	1.4	4	1.9	1.2	4.2	1.6
-20	0.52	3.2×10^{-5}	7.1×10^{-7}	1.62	1.6	4	2.0	1.3	4.0	1.5
-25	0.47	1.0×10^{-4}	8.2×10^{-7}	2.01	2.1	5	2.5	1.5	4.5	1.4
-30	0.41	4.3×10^{-4}	8.5×10^{-7}	2.57	2.9	6	3.1	1.7	4.8	1.4
-35	0.34	2.9×10^{-3}	3.3×10^{-7}	3.48	4.3	7	3.9	2.1	4.9	0.9

an attempt for a conformational readjustment succeeds, which is approximately described by an equation similar to Eq. (1), i.e.,

$$\tau_\alpha \approx \tau^* e^{\Delta F(T)/k_B T}. \quad (20)$$

We note that the T dependence of ΔF confers to Eq. (20) a non-Arrhenius character.

The fitting results reported in Table IV for oriented PVDF, and their comparison with the data listed in Table III, show that at given T the readjustment free energy is larger in the oriented sample. Assuming that the α relaxation is localized within the amorphous layers of the semicrystalline stacks, we may envisage two reasons for the increase of ΔF in the oriented sample at a given T . The first is that the thickness of the amorphous laminar regions is lower than in the case of the isotropic sample, thus implying a more effective confinement with regards to the conformational dynamics. The other is the mean chain orientation in these regions, which previous studies on PET suggest that it may well enhance cooperativity [13,23].

The latter hypothesis finds support from previous investigations on cold drawn PET [50] showing that in an oriented melt, the density autocorrelation length $\xi_{||}$ along the chain direction is larger than the autocorrelation length ξ in an isotropic melt at the same T . By using a Gaussian chain model it was found that $\xi_{||} \approx \kappa^{1/2} \xi$, being κ the drawing ratio [50]. On the other hand, with reference to the analogies relating confined segmental relaxation and the glass transition process, support to the connection between cooperativity enhancement and chain orientation is provided by Ref. [51],

where statistical mechanical calculations show that chain orientation leads to an increase of the glass transition temperature in a polymeric liquid.

Comparing the cooperativities z of the two samples as reported in the Tables III and IV, it is found that $z_{or}/z_{iso} \approx 1.8$ independent of both T and n . This suggests that z_{or}/z_{iso} is mainly determined by geometrical features, i.e., either chain orientation or interlamellar thickness or both, and almost at all by the mode quenching associated to the actual temperature where the relaxation is observed. It is important to stress that the possibility of a confinement effect by crystals on z_{or}/z_{iso} must be taken into account in any case, contrary to what at first glance may seem by considering the results reported in Table IV for $-25 \text{ °C} \leq T \leq -15 \text{ °C}$. Indeed, since the volume occupied by one monomer is $v \approx 0.06 \text{ nm}^3$ (being 64 its molecular weight and the density ρ as given in the experimental section), these latter indicate that the SCRR size is significantly smaller than the interlamellar spacing l_a , which might suggest that, being the crystals far enough apart, their confining effect could be neglected. On the other hand, the ratio z_{or}/z_{iso} still maintains its value, and it would be natural to associate in this case a dominant role in the observed cooperativity enhancement to chain orientation. Actually, this cannot be inferred. Recent literature data analysis (by means of the same model) performed on isothermally crystallized polymers, point out a correlation between the average rearrangement chemical potential barrier $\Delta\mu$ at a given T and the corresponding chemical potential change $\Delta\mu$ of a crystallizing monomer, even when the SCRR size is significantly smaller than the interlamellar spacing [52]. This means that although the crystal surfaces might seem too far apart to influence the relaxation dynamics, in fact they do.

TABLE IV. Same as Table III for oriented semicrystalline PVDF at a temperature of 100 °C.

T (°C)	b	τ_{HN} (sec)	τ^* (sec)	λ (kcal/mol) ⁻¹	z	n	ΔF (kcal/mol)	$\delta(\Delta F)$ (kcal/mol)	$\bar{\zeta}$ (kcal/mol)	$\delta\zeta$ (kcal/mol)
-15	0.42	3.3×10^{-5}	2.9×10^{-7}	1.97	2.4	4	2.6	1.7	3.7	1.4
-20	0.37	8.9×10^{-5}	2.1×10^{-7}	2.38	3.1	5	3.2	2.0	4.2	1.4
-25	0.35	3.2×10^{-4}	2.3×10^{-7}	2.87	3.8	6	3.7	2.1	4.6	1.4
-30	0.29	2.1×10^{-3}	2.9×10^{-7}	3.81	5.3	7	4.3	2.5	4.8	1.4
-35	0.26	8.3×10^{-3}	2.4×10^{-7}	5.57	7.2	9	4.9	2.8	5.4	1.5

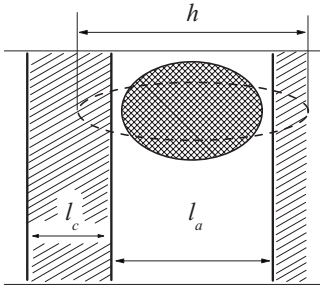


FIG. 11. Schematic of an SCRR within a portion of a stack. The more elongated ellipsoid (dashed line) does not fit into the available interlamellar regions, so the actual shape of the SCRR must be characterized by a lower elongation.

Although it is very likely that, within the interlamellar amorphous layers, a mean chain orientation along the drawing direction establishes in oriented PVDF, the present data cannot provide information in this respect. However, the question rises naturally about the shape that a SCRR may have in this case; should it be somehow related to the auto-correlation length, an ellipsoidal shape would be expected. It is not possible to give an answer here, but the analysis performed on the low- T data (i.e., $T = -30$ and -35 °C) poses lower limits to the possible elongation of a SCRR. To fix our mind, let's imagine an elongated SCRR to be cylindrical in shape, with height h and radius r of the base; then the elongation $\eta \equiv h/r$ can be defined. On the other hand, the drawing ratio of a sample with initial and final lengths ℓ and ℓ_{drawn} respectively, is defined as $\kappa \equiv \ell_{drawn}/\ell$ and of course, h/R would correspond to the drawing ratio of a SCRR, being $R \approx \sqrt[3]{zv}$ the radius of a spherical SCRR of volume zv (i.e., before orientation). The elongation and the drawing ratio are related approximately by $\kappa \approx \eta^{2/3}$. Assume now that an elongation corresponding to the drawing ratio $\kappa = 4$ could be attributed to a SCRR. Then a major axis of $h \geq 3$ nm (at a temperature of -35 °C, where $z = 7.2$) would be found from the approximate formula

$$h \approx \kappa \sqrt[3]{zv}. \quad (21)$$

Since the average interlamellar thickness is $l_a \approx 2.2$ nm, it is evident that the actual elongation factor could not correspond to $\eta \approx \kappa^{3/2} = 8$; that is, $h/R < \kappa$ should hold (see Fig. 11). A similar calculation for $T = -30$ °C would yield $h \geq 2.7$ nm after Eq. (21), i.e., again the SCRR elongation cannot reach $\kappa = 4$.

VI. CONCLUSIONS

Wavelike perturbations carry along by definition a certain order in the motion, e.g., the correlations in molecular displacements along the wave vector direction. In practice, this kind of ordered modes may be active under the condition that these correlations can persist over the distance of some wavelength. The establishing of confinement affects the collective molecular motion through the progressive hindering

of these wave-like modes and the cooperative character of the conformational readjustment dynamics emerges.

As illustrated above, the change in character of the conformational motion is associated to the existence of a wavelength cutoff, quite like in the case of a liquid close to the glass transition. This rather general feature is not the only one shared by these two scenarios (i.e., confined and supercooled liquids); indeed, another aspect has been pointed out by the analysis presented above, namely, that the size of the SCRRs increases upon decreasing T . This mechanism underlies the Adam-Gibbs approach [14,53] for liquids, so it is natural to find it here, given the basis over which the present model has been developed. However, the above analysis points out this feature in the case of confinement induced cooperativity, for the first time and from direct data analysis.

Another aspect needs be stressed, namely, that a connection between fragility parameter and readjustment free energy (and/or its change with T) is worth being investigated. Deeper insights about this issue are not possible presently, but we feel it is important to address the interest toward this issue; this would allow for the connection of a semiempirical parameter like fragility, with physical quantities to which some scientific community might be more accustomed.

With regard to the effect of chain orientation, it was not possible to disentangle it from the enhanced confinement associated to the decrease in interlamellar thickness upon sample stretching. There are of course indications that chain orientation causes an increase of z [13,23,52] (this would also be in agreement with the fact that the glass transition temperature of an oriented liquid should increase [51]) but the present results can only appear consistent with the previous ones. Probably the effect of chain orientation at fixed conditions of physical confinement (see the Introduction) will be pointed out eventually, but different suitable model systems need be considered for this purpose. In particular it would be worth assessing how just the physical confinement affects the conformational relaxation dynamics. In this respect, investigations could be better addressed toward suitable block copolymer systems.

In conclusion, even in the limits of the mean-field nature of the model, the present work pointed out some relations between confined and supercooled liquids which are worth being further investigated. With the aim of elucidating more general aspects of the glass transition, further investigations on confined systems are actually in progress.

ACKNOWLEDGMENTS

The authors thank the financial support from the MICINN (Grants No. MAT2009-07789 and No. MAT2008-03232, and No. PETRI PET2007_0186_03), Spain. A.S. thanks CSIC for the tenure of a JAE-Doc contract. M.P. gratefully acknowledges MCYT for the award of a sabbatical grant (Grant No. SAB-2006-0077) to work at IEM, CSIC, Madrid and CNR, Italy, for supporting this initiative within the framework "Congedi per Motivi di Studio."

- [1] M. Alcoutlabi and G. B. McKenna, *J. Phys.: Condens. Matter* **17**, R461 (2005).
- [2] C. B. Roth and J. R. Dutcher, *J. Electroanal. Chem.* **584**, 13 (2005).
- [3] J. S. Sharp and J. A. Forrest, *Phys. Rev. Lett.* **91**, 235701 (2003).
- [4] C. B. Roth, J. R. Dutcher, and A. G. Marangoni, *Soft Materials: Structure and Dynamics* (Sekker/CRC Press, New York, 2004).
- [5] M. M. Elmahdy, K. Chrissopoulou, A. Afratis, G. Floudas, and S. H. Anastasiadis, *Macromolecules* **39**, 5170 (2006).
- [6] B. Yu, P. Sun, T. Chen, Q. Jin, D. Ding, B. Li, and A. C. Shi, *Phys. Rev. Lett.* **96**, 138306 (2006).
- [7] T. P. Russell, P. Lamboy, G. J. Kellogg, and A. M. Mayes, *Physica B* **213-214**, 22 (1995).
- [8] Y. Zhang, S. Mukoyama, Y. Hu, C. Yan, Y. Ozaki, and I. Tatakahashi, *Macromolecules* **40**, 4009 (2007).
- [9] G. Reiter, I. Botiz, L. Gravelleau, N. Grozev, K. Albrecht, A. Mourrán, and M. Möller, *Progress in Understanding of Polymer Crystallization* (Springer Distribution Center GmbH, Heidelberg, Germany, 2007).
- [10] Y.-S. Sun, T.-M. Chung, Y.-J. Li, R.-M. Ho, B.-T. Ko, U.-S. Jeng, and B. Lotz, *Macromolecules* **39**, 5782 (2006).
- [11] M. Beiner, *J. Polym. Sci., Part B: Polym. Phys.* **46**, 1556 (2008).
- [12] V. Crupi, D. Majolino, P. Migliardo, and V. J. Venati, *J. Mol. Struct.* **448**, 255 (1998).
- [13] M. Pieruccini and T. A. Ezquerra, *Eur. Phys. J. E* **29**, 163 (2009).
- [14] G. Adam and J. H. Gibbs, *J. Chem. Phys.* **43**, 139 (1965).
- [15] F. Stickel, F. Kremer, and E. W. Fische, *Physica A* **201**, 318 (1993).
- [16] F. Kremer, A. Huwe, M. Arndt, P. Behrens, and W. Schwieger, *J. Phys.: Condens. Matter* **11**, A175 (1999).
- [17] D. Kranbuehl, R. Knowles, A. Hossain, and A. Gilchrist, *J. Non-Cryst. Solids* **307-310**, 495 (2002).
- [18] J. A. Forrest, K. Dalnoki-Veress, and J. R. Dutcher, *Phys. Rev. E* **56**, 5705 (1997).
- [19] D. Labahn, R. Mix, and A. Schoenhals, *Phys. Rev. E* **79**, 011801 (2009).
- [20] S. Napolitano, V. Lupascu, and M. Wubbenhorst, *Macromolecules* **41**, 1061 (2008).
- [21] Z. Hu, M. Tian, B. Nysten, and A. M. Jonas, *Nature Mater.* **8**, 62 (2009).
- [22] J. Martin, C. Mijangos, A. Sanz, T. A. Ezquerra, and A. Nogales, *Macromolecules* **42**, 5395 (2009).
- [23] M. Pieruccini, T. A. Ezquerra, and M. Lanza, *J. Chem. Phys.* **127**, 104903 (2007).
- [24] R. J. Young, *Introduction to Polymers* (Chapman and Hall, London, 1981).
- [25] S. Havriliak and S. Negami, *Polymer* **8**, 161 (1967).
- [26] K. U. Kirst, F. Kremer, and V. M. Litinov, *Macromolecules* **26**, 975 (1993).
- [27] E. Ozkazanc, H. Y. Guney, T. Oskay, and E. Tarcan, *J. Appl. Polym. Sci.* **109**, 3878 (2008).
- [28] J. B. Enns and R. Simha, *J. Macromol. Sci., Phys.* **13**, 25 (1977).
- [29] S. Osaki and Y. Ishida, *J. Polym. Sci., Polym. Phys. Ed.* **13**, 1071 (1975).
- [30] A. J. Lovinger, *Developments in Crystalline Polymers* (Applied Science Publications, London, 1981).
- [31] M. C. García-Gutiérrez, J. J. Hernández, A. Nogales, P. Paine, D. R. Rueda, and T. A. Ezquerra, *Macromolecules* **41**, 844 (2008).
- [32] A. Nogales, I. Sics, T. A. Ezquerra, Z. Denchev, F. J. Baltá Calleja, and B. S. Hsiao, *Macromolecules* **36**, 4827 (2003).
- [33] G. R. Strobl and M. Schneider, *J. Polym. Sci., Polym. Phys. Ed.* **18**, 1343 (1980).
- [34] J. Wing Sy and J. Mijovic, *Macromolecules* **33**, 933 (2000).
- [35] J. Mijovic, J.-W. Sy, and T. K. Kwei, *Macromolecules* **30**, 3042 (1997).
- [36] J. C. Coburn and R. H. Boyd, *Macromolecules* **19**, 2238 (1986).
- [37] A. Nogales, Z. Denchev, I. Sics, and T. A. Ezquerra, *Macromolecules* **33**, 9367 (2000).
- [38] N. G. McCrum, B. E. Read, and G. Williams, *Anelastic and Dielectric Effects in Polymeric Solids* (Dover, New York, 1991).
- [39] R. Böhmer, K. L. Ngai, C. A. Angell, and D. J. Plazek, *J. Chem. Phys.* **99**, 4201 (1993).
- [40] R. Böhmer and C. A. Angell, *Phys. Rev. B* **45**, 10091 (1992).
- [41] R. Böhmer, *J. Non-Cryst. Solids* **172-174**, 628 (1994).
- [42] S. V. Nemilov, *J. Non-Cryst. Solids* **352**, 2715 (2006).
- [43] R. Richert and C. A. Angell, *J. Chem. Phys.* **108**, 9016 (1998).
- [44] C. A. Angell, *Polymer* **38**, 6261 (1997).
- [45] C. A. Angell, *J. Non-Cryst. Solids* **131-133**, 13 (1991).
- [46] O. N. Senkov, *Phys. Rev. B* **76**, 104202 (2007).
- [47] J. Dudowicz, K. F. Freed, and J. F. Douglas, *J. Chem. Phys.* **123**, 111102 (2005).
- [48] J. Dudowicz, K. F. Freed, and J. F. Douglas, *J. Phys. Chem. B* **109**, 21350 (2005).
- [49] G. Williams, *Chem. Rev.* **72**, 55 (1972).
- [50] F. J. Baltá Calleja, G. Di Marco, A. Flores, and M. Pieruccini, *Phys. Rev. B* **75**, 224201 (2007); **79**, 019903(E) (2009).
- [51] J. H. Gibbs, *J. Chem. Phys.* **25**, 185 (1956).
- [52] M. Pieruccini and A. Flores, *Colloid Polym. Sci.* **288**, 365 (2010).
- [53] P. G. Debenedetti, *Metastable Liquids: Concepts and Principles* (Princeton University Press, Princeton, NJ, 1996).